PREPRINT. Accepted for publication
in Computational Geosciences

Computational Geosciences manuscript No.
(will be inserted by the editor)

Low dispersive modeling of Rayleigh waves on Partly-Staggered grids

O. Rojas · B. Otero · J. E. Castillo · S. M. Day

Received: date / Accepted: date

Abstract In elastic media, finite difference (FD) implementations of free surface (FS) boundary conditions on Partly-Staggered Grids (PSG) use the highly dispersive vacuum formulation (VPSG). The FS boundary is embedded into a "vacuum" grid layer (null Lame constants and negligible density values) where the discretized equations of motion allow computing surface displacements. We place a new set of Compound (stress-displacement) nodes along a planar FS and use unilateral mimetic FD discretization of the zero-traction conditions for displacement computation (MPSG). At interior nodes, MPSG reduces to standard VPSG methods and applies fourth-order centered FD along cell diagonals for staggered differentiation combined with nodal second-order FD in time. We perform a dispersion analysis of these methods on a Lamb's problem and estimate dispersion curves from the phase difference of windowed numerical Rayleigh pulses at two FS receivers. For a given grid sampling criterion (e.g., 6 or 10 nodes per reference S wavelength λ^S), MPSG dispersion errors are only a quarter of the VPSG method. We also quantify root-mean-square (RMS) misfits of numerical time series relative to analytical waveforms. MPSG RMS misfits barely exceed 10% when 9 nodes sample the minimum S wavelength λ^S_{MIN} in transit (along distances $\sim 145\lambda^S_{MIN}$). In same tests, VPSG RMS misfits exceed 70%. We additionally compare MPSG to a consistently fourth-order mimetic method designed on a Standard Staggered Grid. The latter equates former's dispersion errors on grids twice denser, and shows higher RMS precision only on grids with 6 or less nodes per λ^S_{MIN}.

Keywords Staggered grid · high-order modeling · finite difference · wave equation

Mathematics Subject Classification (2000) 35A24 · 35L02 · 65L12 · 81T80

O. Rojas
Universidad Central de Venezuela, Caracas, Venezuela
Tel.: +058-416-5380442 - +058-212-6051264
Fax: +058-212-6051131
E-mail: rojasotilio@gmail.com

B. Otero
Universitat Politécnica de Catalunya-TECH, Barcelona, Spain
Tel.: +034-93-4054046 - +034-636557161
Fax: +034-93-4017055
E-mail: botero@ac.upc.edu

J. E. Castillo
San Diego State University, California, USA
E-mail: jcastillo@sdsu.edu

S. M. Day
San Diego State University, California, USA
E-mail: day@moho.sdsu.edu

1 Introduction

Modern finite differences (FD) methods in computational seismology use a Cartesian Staggered Grid (SG) for domain and wavefield discretization. In a SG, material parameters are defined on individual rectangular meshes displaced by half of the grid spacing in one or more directions. Similar staggering distribution is used to locate each wavefield at the center of those it depends upon, and numerical differentiation gains accuracy by halving the grid spacing. A widely used SG on elastic wave propagation collocates each displacement (or particle velocity) component and each shear stress at a distinct grid site. Only normal stresses are placed at the same grid location given its common dependency on all diagonal strain components. This grid has been referred as Standard Staggered Grid (SSG) by Moczo et al. [27] and Saenger et al. [36]. Pioneering

works of Madariaga [24], Virieux [37][38], Levander [21], Graves [16], and Kristek et al. [19] have brought clarity on the implementation details for precise modeling of elastic motion in 2-D and 3-D heterogeneous media that might include subsurface topography and planar Free Surface (FS) boundaries. The competing type of SG is the Partly-Staggered Grid (PSG), so called because all displacement (or particle velocity) components share the same grid location, that is displaced by half of the grid spacing in all coordinate directions of the common site of all stress components. Early applications of PSG on modeling fault rupture propagation were performed by Andrews [2] and Day [11][12], in 2-D and 3-D media, respectively. Later, Zhang [40] developed a 2-D velocity-stress FD method for elastic motion on PSG. Saenger et al. [36], Saenger and Bohlen [35], and Bohlen and Saenger [3] used PSG in simulations of elastic and viscoelastic wave propagation in the presence of material heterogeneities, cracks, and FS. Instead of PSG, these authors employed the alternative names of "rotated" and "modified" SG to refer to this grid type attending to the numerical differentiation procedure along cell diagonals. Recently, Cruz-Atienza et al. [9][10] have modeled dynamic earthquake ruptures along non planar faults employing PSG.

Modeling of FS boundary conditions has been a long explored component of FD SG methods because the process of zeroing traction components and computing particle displacements (or velocities) at this interface is highly dependent on the distribution of material properties and wave fields throughout the grid. In the classical vacuum formulism, a thin grid layer is defined above this boundary where Lame parameters are zeroed. Thus, the traction vector implicitly vanishes along all stress tensor components, including those that are not constrained by the zero traction condition. In most accurate implementations, the density is set in this "vacuum" layer at a value much smaller than the actual density of the solid layer underneath (of the order of $10^{-3}\,\frac{kg}{m^3}$), and displacements (or velocities) are locally computed by using second-order discretizations of the equation of motion. The use of higher-order approximations leads to numerical instabilities on both types of grids SSG ([16]) and PSG ([35][14]). Some early applications on the former grids showed significant inaccuracies of the vacuum method, and authors claim that keeping a nonzero density value above the FS implies an inappropriate reflection coefficient along this boundary, and then energy leaks to the fictitious vacuum ([16][39]). As a reference test, Graves [16] presents 3-D simulations of surface waves induced by a superficial source along a planar FS, where the amplitude of Rayleigh pulses is poorly modeled at short epicentral distances of approximately $9\lambda^S_{MIN}$ (minimum S wavelength), even though he employed a SSG that supported 9.2 grid points per λ^S_{MIN}. After Graves's work, the use of the vacuum formulation was largely abandoned on SSG in favor of emerging and more precise FS implementations like the Imaged-Stress Method and the Adjusted FD Approximation, both commented upon below. On the other hand, the vacuum method represents the dominant implementation strategy of FS boundaries into current elastic and viscoelastic wave propagation FD methods on PSG ([36][3][14][8]). On 2-D tests along planar FS, Bohlen and Saenger [3] mitigate the accuracy loss driven by grid dispersion on Rayleigh waves by refining the grid up to fit at least 17 nodes per minimum Rayleigh wavelength λ^R_{MIN}, and obtain precise propagation along distances of approximately $18\lambda^R_{MIN}$. These authors employed even more refined PSG on experiments with dipping planar FS. To gain accuracy on the vacuum FS implementation with variable topography on coarser grids, Lombard et al. [22] propose a modified 2-D PSG with all wavefield variables located at a common grid point (grid is no longer staggered), time stepped by a combination of extrapolation and integration techniques. On tests where a straight FS is inclined by various angles, they achieved stable and accurate results using 10 grid points per λ^S_{MIN} along propagating distances of $50\lambda^S_{MIN}$.

A less dispersive FD implementation of planar FS on SSG is the stress-imaging formulation introduced in elastic media by Levander [21] in 2-D, and later adapted to 3-D by Rodrigues [31] and Graves [16]. This approach also extends the SG beyond the FS boundary for a few grid levels, and uses this boundary as an antisymmetry mirror for stress components conditioned by the nullity of the traction vector. At FS grid points, such stresses are directly zeroed, while their values are chosen as the antisymmetric image of their interior counterparts at nodes above of it (to average zero at FS). Remaining stresses and particle displacements (or velocities) in the FS grid vicinity are computed by FD discretizations of stress-strain and momentum equations, where stencils crossing the FS are limited to second-order (see [19], for implementation details). Planar FS can be naturally accommodated along either of two grid planes of a SSG and we assume a Cartesian (x, y, z) reference system to describe them. In one implementation, the FS coincides with the plane placing (xx, yy, zz) normal stresses and both tangential components of the displacement (or velocity) vector. The second implementation defines the FS as the grid plane that holds the transverse component of the displacement (or velocity) vector and both (xz, yz) shear stresses. Kristek et al. [19] referred to the former alternative as the *H-formulation*,

while *W-formulation* was the name given to the latter. Graves [16] compares the *H-formulation* of the image method to the vacuum strategy in the same test referred above (under a grid resolution of 9.2 points per λ^S_{MIN}) and observes a more precise modeling of surface wave amplitudes by the former. Bohlen and Saenger [3] also present 2-D comparisons of both competing FS formulations, and conclude that stress imaging on SSG requires half the grid sampling of the vacuum method to obtain similar precision on Rayleigh propagation on PSG (9 nodes versus 17 nodes, per λ^R_{MIN}, respectively). Alternatively, Kristek et al. [19] focused on assessing both *H-* and *W- formulation* of the image method on 3-D SSG and used a near-surface Gabor wavelet to excite strong surface waves on a homogeneous halfspace; separate tests were performed for Poisson ratio values of 0.25, and 0.45. In these experiments, they found that both formulations require a minimum of 10 nodes per λ^S_{MIN} to achieve low dispersive propagation of Rayleigh waves in the range of epicentral distances up to $22.5\lambda^S_{MIN}$, and these results are practically independent of the Poisson ratio. Further applications and assessments of the stress imaging formulation on planar FS can be found in Robertson [30]; Pitarka [29]; Gottschammer and Olsen [15]; and Olsen et al. [28]. This approach also offers the flexibility to accommodate realistic Earth's topography and extensions to non planar FS have been proposed by Jih et al. [17], Tessmer and Kosloff [18], and Zhang and Chen [6].

For planar FS, Kristek et al. [19] propose the *H-* and *W- formulations* of the Adjusted FD Approximations (AFDA) on 3-D SSG, both carefully designed to compute particle velocities and stress components with fourth-order accuracy at the FS and grid planes nearby. In these formulations, no fictitious grid planes are defined outside the FS because spatial discretization of Hooke's laws and equations of motions uses unilateral stencils on the FS normal direction combined to central stencils on the tangential direction to this boundary. This stencil combination makes these formulations more efficient than the image method, as experimentally shown by Kristek et al. [19] (same experiment detailed above). There, AFDA methods only required 6 grid points per λ^S_{MIN} to model Rayleigh wave propagation with similar accuracy of the imaging technique. Therefore, grid sampling needs of AFDA formulations are comparable to the grid resolution demands of fourth-order SG methods for precise propagation of body waves at interior nodes (Moczo et al., [26][25]).

This paper presents two contributions to the modeling of surface waves along a planar FS. The first one, is an elastodynamics FD solver on a 2-D PSG that replaces the vacuum method by an explicit discretization of zero traction conditions on a new set of single grid nodes (holding all displacement and stress components) that we call *Compounds*. In our PSG, the FS grid plane is comprised of only Compound nodes. At each of these nodes, second-order unilateral FD boundary conditions (zero zz and xz stresses) along the rotated axes allow computing both FS displacements, once interior displacements are time stepped at grid lines nearby. At interior grid points, spatial discretization of all wavefields is fourth-order accurate. This new FS formulation avoids fictitious grid points, and instead explicitly discretizes the null traction conditions by unilateral FD in a manner similar to that used by AFDA on SSG. However, our discretization uses the *mimetic* or conservative FD operators proposed by Castillo and Grone [4] that combine one-sided and central stencils on a 1-D SG, with separate order of accuracy (between second- and fourth- order) at boundary and interior nodes. We call this *mimetic* FD method MPSG. We additionally test a fourth-order accurate version of our MPSG FS formulation, but unfortunately boundary computations degenerate in numerical instabilities. The second contribution of this paper is a simple procedure to isolate the Rayleigh pulse from a surface-wave time series excited on a homogeneous halfspace, and computation of the corresponding phase speed via fast Fourier transform (*fft*). Then, the Dispersion Curve of the Rayleigh (DCR) wave can be obtained from the phase differences at two surface receivers along waves' path. Based on this procedure, we compare DCR from the vacuum and MPSG methods when solving the classical Lamb's problem and quantify accuracy of both in terms of grid sampling of reference λ^S.

2 Problem Formulation

In this section, we present the mathematical formulation of the 2-D wave propagation problem used in our numerical studies. We consider a linearly elastic and isotropic half plane with a horizontal axis x ($-\infty < x < \infty$) and a vertical axis z positive downward ($-\infty < z \leq 0$). We take the plane $z = 0$ as the interface with a vacuum layer that we refer as free surface (FS). Particle motion is described by the elastodynamic wave equation,

$$\rho\ddot{u} = \tau_{xx'x} + \tau_{xz'z} \tag{1}$$

$$\rho\ddot{w} = \tau_{zz'z} + \tau_{xz'x} \tag{2}$$

and the constitutive stress-strain relationships (Hooke's law),

$$\tau_{xx} = (\lambda + 2\mu)u_{'x} + \lambda w_{'z} \tag{3}$$

$$\tau_{zz} = (\lambda + 2\mu) w_{\prime z} + \lambda u_{\prime x} \quad (4)$$

$$\tau_{xz} = \mu (u_{\prime z} + w_{\prime x}) \quad (5)$$

Here, we adopt the notation $\ddot{u} = \frac{\partial^2 u}{\partial t^2}$, $u_{\prime x} = \frac{\partial u}{\partial x}$, $\tau_{xx\prime x} = \frac{\partial \tau_{xx}}{\partial x}$ and so on, where t represents physical time. Dependent variables are the components of the displacement vector $\mathbf{u}= (u, w)$, and the symmetric stress tensor with diagonal components τ_{xx}, and τ_{zz}, and off-diagonal component τ_{xz}. In this model, medium parameters are the density ρ and Lame constants λ and μ. Solution of eqns. (1) to (5) requires appropriate initial and boundary conditions. In this work, we assume quiescence prior to wave excitation at $t = 0$, thus $\mathbf{u}=\dot{\mathbf{u}}=\mathbf{0}$ everywhere for $t \leqslant 0$, and traction must be null at the FS for $t \geqslant 0$, i.e.,

$$\tau_{zz} = \tau_{xz} = 0, \; at \; z = 0 \quad (6)$$

Material particles move in response to three types of waves coexisting in our simplified model. The scalar compressional (P) wave and the vertical component of the shear (SV) wave, with speeds denoted as V_P and V_S, respectively, that correspond to $V_P = \sqrt{\frac{\lambda+2\mu}{\rho}}$ and $V_S = \sqrt{\frac{\mu}{\rho}}$. The interaction of both body waves P and SV with the FS excites Rayleigh pulses that propagate at speed V_R dependent on V_P and V_S. A Rayleigh wave is a known example of surface waves because their amplitudes decay rapidly with depth. Love surface waves and body SH waves also present in more general tridimensional applications are absent in our simplified 2-D model, but the new numerical method described in next sections are naturally extensible to 3-D rectangular domains.

3 Vacuum formulism on a Partly-Staggered Grid: VPSG scheme

We first implement the zero traction boundary conditions on a planar FS of a 2-D elastic medium using the Vacuum method and a PSG with the purpose of obtaining reference solutions for comparative accuracy studies against our new method. Here, we name this implementation as VPSG and follow Gelis et al. [14] and Cruz-Atienza [7] for algorithmic details. Figure 1 depicts a typical PSG composed by only two types of nodes, displacement and stress gridpoints, each of them locating all components of the respective physical quantity. As shown, density and Lame parameters are separately placed at every displacement node and stress node, respectively. The dotted line represents the FS boundary defined along the first line of stress nodes at which null Lame values are imposed. This leads to zeroing traction components τ_{zz} and τ_{xz}, as well as the stress τ_{xx} which is not physically constrained by the planar FS boundary condition. Displacements u and w are also zeroed at the gridline above the FS in correspondence with the nullity of the Lame parameters in the Vacuum layer. In the computation, FS displacements correspond to those computed at nodes half-way below the zero-stress gridline. We would like to point out that an alternative Vacuum implementation is given by setting the FS boundary on a displacement (or velocity) grid line above which zero stresses implicitly enforce traction nullity (see, for instance [3]). However, in this work we only consider the former VPSG implementation detailed above in our numerical studies.

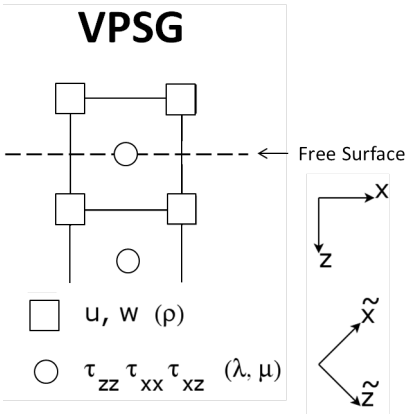

Fig. 1: Partly-Staggered Grid with a FS boundary condition implemented by vacuum formulation. Squares represent displacement nodes where density is also defined, and circles correspond to stress nodes where Lame parameters are assumed available. Dashed lines denote the FS boundary above which zero-displacement grid nodes are also defined

To further detail our VPSG implementation in a Cartesian grid with steps Δx and Δz, we introduce a set of coordinate axes ($\check{x}$,$\check{z}$) by rotating the original axes (x,z) by $\tan^{-1}\frac{\Delta z}{\Delta x}$ degrees. This implies that new rotated axes are aligned with the diagonals of grid cells, and spatial differentiation can proceed along $\check{x}$ and $\check{z}$ directions employing finite difference (FD) staggered stencils with the cell diagonal Δr as the spatial step. Saenger et al. [36] expresses the relationships between grid steps and partial derivates on both coordinate systems as follow

$$\check{z} = \frac{\Delta x}{\Delta r} x + \frac{\Delta z}{\Delta r} z; \check{x} = \frac{\Delta x}{\Delta r} x - \frac{\Delta z}{\Delta r} z; \Delta r^2 = \Delta x^2 + \Delta z^2 \quad (7)$$

$$\frac{\partial}{\partial z} = \frac{\Delta r}{2\Delta z}\left(\frac{\partial}{\partial \check{z}} - \frac{\partial}{\partial \check{x}}\right); \frac{\partial}{\partial x} = \frac{\Delta r}{2\Delta x}\left(\frac{\partial}{\partial \check{z}} + \frac{\partial}{\partial \check{x}}\right) \quad (8)$$

Numerical differentiation on VPSG, as well as on previous PSG elastic or viscoelastic solvers, is carried

out along cell diagonals to approximate derivatives with respect to rotated coordinates ($\check{x}$,$\check{z}$). Then, these approximations are transformed into the original coordinates (x,z) by equation (8) to solve the equations of motion (1) to (5), which always remain in the Cartesian system. Second-order and fourth-order FD stencils correspond to the standard SG differentiators $\Delta r^{-1}(-1,1)$, and $(24\Delta r)^{-1}(1,-27,27,-1)$, respectively (see for instance, Levander [21]). To compute FS displacements along the gridline buried by $\frac{\Delta z}{2}$, second-order SG stencils are used for stress differentiation in (1) and (2), followed by the standard nodal-centered discretization of time derivates by means of the stencil $\Delta t^{-2}(1,-2,1)$. At this grid level, we verify that using instead fourth-order unilateral SG differentiators for stress fields (as those given by first row on matrix D_{4-4} in Appendix A) trigger numerical instabilities. However, both second- and fourth- order centered SG stencils describe above can be applied for displacement differentiation along the first interior stress line and simulation remains stable. Thus, we choose the fourth- order SG stencil for our VPSG implementation, and same stencil in then used to differentiate any wavefield at grid lines below. Also, time differentiation of acceleration terms in (1) and (2) is performed anywhere by the nodal stencil referred above.

Numerical stability and grid dispersion of PSG FD methods was recently reviewed by Saenger et al. [36] in the case of an unbounded homogeneous and elastic medium. For a second-order accurate scheme in time, they found the following Von-Neumann stability bound for the time step Δt

$$\frac{\Delta t\, V_p}{\Delta h} \leqslant \frac{1}{\Sigma_{K=1}^{n}|C_K|}, \tag{9}$$

where scalars C_K are the coefficients of the (2n)th-order accurate central stencil for SG differentiation in space ($n \geqslant 1$), and Δh represents the common grid step on both directions (x,y) on a square PSG (i.e., $\Delta h = \Delta x = \Delta z$). Interestingly, above stability constraint (9) results the same for 2-D and 3-D PSG. Although, this Von-Neumann bound omits the existence of a FS boundary and surface waves in our P-SV model, we here use it to limit the time step Δt in our VPSG simulations.

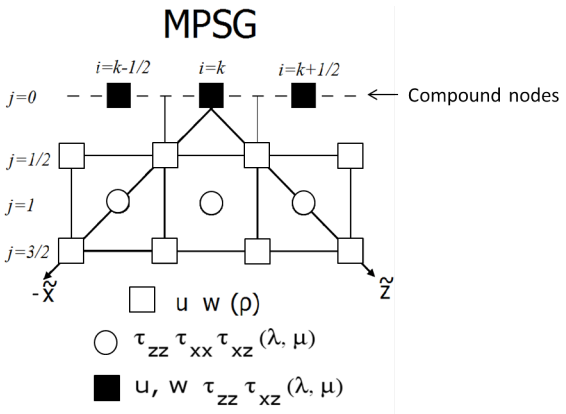

Fig. 2: Adapted Partly-Staggered Grid for *mimetic* discretization. Interior grid distribution of wavefield components and material properties is identical to figure 1. The FS boundary (dashed line) is discretized by the Compound nodes (filled squeares) that locate all displacement and stress tensor components. The rotated axes have been included to illustrate the differentiation directions at Compound nodes

4 Mimetic operators on a Partly-Staggered Grid: MPSG scheme

The formulation of our numerical scheme begins by representing a planar FS on a PSG by a new grid line of single nodes that place all displacement and stress components (filled squares in figure 2). We have called these special boundary gridpoints *Compound nodes*. Reader might picture this single Compound gridline in figure 2 as the merging of both (fictitious displacement and FS stress) gridlines that comprise the Vacuum layer in figure 1.

Notice that along any rotated ($\check{x}$,$\check{z}$) coordinate line of this new PSG, the grid reduces to a 1-D SG with three different types of nodes: displacement, stress, and Compound gridpoints; where the latter is placed at the boundary. This wavefield grid distribution facilitates the application of unilateral SG FD stencils (along rotated axes) at compound nodes and neighbor gridpoints, leading to an explicit discretization of FS conditions at the Compound nodes. To do so, we adopt the FD *mimetic* operators proposed by Castillo and Grone in [4] on a 1-D SG that corresponds to any gridline along either $\check{x}$ or axis $\check{z}$. Castillo-Grone operators offer adjustable order of accuracy with either second- or fourth-order differentiation at boundaries, combined with fourth-order accurate stencils at interior nodes. These operators are given in Appendix A, where sub-indexes "2-4" and "4-4" denote the nominal accuracy at boundary and interior points, respectively. Mimetic operator G comprises SG stencils to suitably perform displacement differentiation along any of the rotated axes, while mimetic operator D can be used for stress staggered differentiation in either rotated direction. Castillo-Grone operators were successfully applied on 2-D SSG by Rojas and collaborators for modeling P-SV motion [32] and dynamic ruptures [33] [34].

We next detail the second-order MPSG discretization of zero traction conditions at FS Compound nodes using mimetic G_{2-4}. In figure 2, gridlines are indexed in both directions x and z by either integer or half-integer numbers to emphasize the staggered nature of this mesh. The application of unilateral stencil (g_{11}, g_{12}, g_{13}) (first row of G_{2-4}) along both rotated directions $\check{x}$ and $\check{z}$ to the displacement u at FS node $(i,0)$, followed by the transformation back to original (x,z) axes, yield the following approximations to first derivates

$$[u\prime_z]_{i,0} = \frac{\Delta r}{2\Delta z}\{2g_{11}u_{i,0} + g_{12}\{u_{i+\frac{1}{2},\frac{1}{2}} + u_{i-\frac{1}{2},\frac{1}{2}}\} + g_{13}\{u_{i+\frac{3}{2},\frac{3}{2}} + u_{i-\frac{3}{2},\frac{3}{2}}\}\} \quad (10)$$

$$[u\prime_x]_{i,0} = \frac{\Delta r}{2\Delta x}\{g_{12}\{u_{i+\frac{1}{2},\frac{1}{2}} + u_{i-\frac{1}{2},\frac{1}{2}}\} + g_{13}\{u_{i+\frac{3}{2},\frac{3}{2}} + u_{i-\frac{3}{2},\frac{3}{2}}\}\} \quad (11)$$

Substitution of approximations (10) and (11), and ones equivalents for displacement w, into the zero traction conditions $\tau_{xz} = \tau_{zz} = 0$, leads to a linear dependence of FS solutions $u_{i,0}$ and $w_{i,0}$ on interior displacements, i.e.,

$$u_{i,0} = -\frac{1}{2g_{11}}\{g_{12}\{u_{i+\frac{1}{2},\frac{1}{2}} + u_{i-\frac{1}{2},\frac{1}{2}}\} + g_{13}\{u_{i+\frac{3}{2},\frac{3}{2}2} + u_{i-\frac{3}{2},\frac{3}{2}}\} + \frac{2\Delta z}{\Delta r}[w\prime_x]_{i,0}\} \quad (12)$$

$$w_{i,0} = -\frac{1}{2g_{11}}\{g_{12}\{w_{i+\frac{1}{2},\frac{1}{2}} + w_{i-\frac{1}{2},\frac{1}{2}}\} + g_{13}\{w_{i+\frac{3}{2},\frac{3}{2}} + w_{i-\frac{3}{2},\frac{3}{2}}\} + \frac{2\Delta z}{\Delta r}\gamma[u\prime_x]_{i,0}\} \quad (13)$$

where $\gamma = \frac{\lambda}{\lambda+2\mu}$. Above equations (12) and (13) allow the time evolution of FS displacements $u_{i,0}$ and $w_{i,0}$, if those are preceded by the updating of interior displacements based on the discretization in space and time of momentum equations (1) and (2). The MPSG pseudocode (Algorithm 1) sketches a time iteration of this scheme where displacements are assumed available at time level $t = n\Delta t$.

An important theoretical concern on MSPG implementation is the impact of the half-way gridline of Compound nodes on the numerical stability of this method, and how it compares to a standard Vacuum-layer algorithm such as VPSG. In our numerical tests (described below), we set time step Δt according to Von-Neumann condition (9) ($\Delta t \sim 0.65\frac{\Delta h}{V_P}$) where C_K are given by the fourth-order SG stencil used at interior differentiation, and observed stable calculations of all wavefields by both schemes during the whole simulation time ($\sim 10000\Delta t$). However, we would like to stress that a general theoretical stability study for MPSG is necessary and viable given the linearity of the P-SV model. A fully fourth-order accurate version (in space) of MPSG is easily implemented by substituting operators G_{2-4} and D_{2-4} in favor of higher-order ones G_{4-4} and D_{4-4} (see Appendix A), respectively, in equations (12)-(13) and MPSG pseudocode. However, in our numerical experiments that use superficial point sources, we observe exponentially growing instabilities in FS displacements $u_{i,0}$ and $w_{i,0}$ right after surface waves pass by. This unfortunate behavior is slightly diminished by an exhaustive reduction of Δt far below the upper limit established by condition (9). Thus, the only available stable implementation of MPSG is the one using second-order spatial differentiation at FS Compound nodes and one gridline below. As a way to incorporate a fourth-order P-SV solver into our dispersion and accuracy assessment of VPSG and MPSG schemes (presented below), we consider the *Mimetic* scheme formulated on a *Standard Staggered* Grid (MSSG method) that was proposed by Rojas in [32]. MSSG corresponds to a fully fourth-order (in space) and stable H-formulation of the zero-traction FS conditions on a 2-D SSG that exploits unilateral differentiation (in the FS normal direction) to evade fictitious gridpoints. Roughly speaking, MSSG might be considered as a simplified 2-D version of the H-AFDA method developed by Kristek and co-workers [19] for planar FS in 3-D elastic media. However, our MSSG scheme differs from the latter method in two aspects: (i) Mimetic formulas replace the traditional Taylor-based stencils used in H-AFDA, and (ii) MSSG computes both displacement components along the FS because of the addition of Compound nodes to a 2-D SSG. H-AFDA does not calculate the displacement component normal to the FS exactly at this boundary, and requires of interpolations to approximate this wavefield from inte-

Algorithm 1 MPSG algorithm: Three-step time evolution

STEP I (stresses at time $t = n\Delta t$): Compute τ_{xx}, τ_{zz} and τ_{xz} at any interior stress nodes ($j \geqslant 1$) by using Hooke's law (3) to (5). Operator G_{2-4} is applied for displacement differentiation along both directions and followed by the transformation (8). FS stresses are given by boundary condition (6) and the fact $\tau_{xx} = (\lambda - \lambda\gamma + 2\mu)u\prime_x$.
STEP II (Interior displacements at $t = (n+1)\Delta t$): Solve (1) and (2) to obtain u and w at every interior displacement node ($j \geqslant \frac{1}{2}$). Operator D_{2-4} is applied for stress differentiation along $\check{x}$ and $\check{z}$ axes and then transformation (8) is used. Time discretization applies nodal stencil $\Delta t^{-2}(1,-2,1)$.
STEP III (FS displacements at $t = (n+1)\Delta t$): Use equations (12) and (13) and interior displacements from *STEP II* to calculate u and w at every Compound node.

rior values. The MSSG scheme is briefly described in Appendix B.

5 Error metrics on frequency and time domains: Lamb's problem

Lamb's problem is a benchmark test used to assess the efficacy of numerical implementations of free-surface boundary conditions on elastic media (e.g., [38] [3] [23] [13]). The response of a homogeneous half-plane due to the application of a vertical point force $f(t)$ at $(x_S, 0)$ is analytically known [1], and exhibits strong and dispersionless Rayleigh waves. Thus, time series of exact displacements (or particle velocities) and corresponding spectral phase speeds can be used as a reference to quantify numerical misfits in both domains, time and frequency. In particular, numerical inaccuracies on modeling the amplitude of Rayleigh waves are better realized on seismograms recorded at free surface receivers given the exponential decay of analytical Rayleigh pulses with depth.

In this section, we describe a new procedure that estimates the phase speed $C(f)$ of Rayleigh pulses windowed on numerical surface waves, and sketches dispersion curves $\frac{C(f)}{C_0}$ using as a reference the constant speed C_0 of all frequency components of the exact Rayleigh pulses. This procedure represents a computational implementation of the two-station dispersion analysis applied to field records of surface waves and discussed in many seismological textbooks (i.e., [20]). For a sufficient time separation between earlier body-wave arrivals and the trailing Rayleigh pulse, our procedure is an easily-coded dispersion analysis tool with no sensitivity to variation of the material Poisson ratio or time shape of the impulsive source. Alternatively, to assess numerical elastic solvers described in previous sections, we also apply a time-dependent error metric to whole waveforms by calculating root-mean-square (RMS) differences of numerical solutions with respect to exact seismograms at certain surface receivers. For instance, let us denote the numerical waveform computed at a receiver location R as $u_R^{NUM}(t_k)$, in the case of the horizontal component of the displacement vector, for discrete times $t_k = k\delta t$, for $k = 0, 1, 2, \ldots$. We use a similar designation for the analytical displacement time series at same location R, $u_R^{AN}(t_k)$, after replacing the superindexed string "NUM" by "AN". Relative RMS misfits of the numerical waveform against its analytical counterpart results,

$$RMS(u_R^{AN}(t), u_R^{NUM}(t)) = \sqrt{\frac{\sum_k \left[u_R^{NUM}(t_k) - u_R^{AN}(t_k)\right]^2}{\sum_k \left[u_R^{AN}(t_k)\right]^2}} \quad (14)$$

Similarly, time-dependent errors on numerical approximations to the vertical displacement component w at superficial receivers are measured by using the same relative RMS metric (eqn. (14)).
Figure 3 illustrates the distribution of eight free-surface receivers denoted by R0, R1, R2,..., R7, respectively, displaced from the source point by epicentral distances ranging from 4.8 km up to 30 km. In our tests described below, the medium is a homogeneous half space with fixed density $\rho = 2500\frac{kg}{m^3}$ and S-wave speed $V_S = 2000\frac{m}{s}$. However, we might vary the Poisson ratio σ and therefore, P wave (V_P) and Rayleigh wave (C_0) speeds are adjusted accordingly. In addition, our tests include variation of the time shape of the impulsive source $f(t)$.

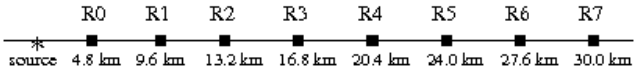

Fig. 3: Geometrical description of our Lamb's test problem. The domain is a homogeneous halfplane and the point source $f(t)$ is applied at $x = 0$

5.1 Dispersion curves of numerical Rayleigh waves: DCR algorithm

The first step of our dispersion analysis procedure is the isolation of the Rayleigh pulse from P and S waves traveling ahead along the FS. To illustrate this step, we calculate the analytical time series of both displacements at receiver R2, $u_{R2}^{AN}(t_k)$ and $w_{R2}^{AN}(t_k)$, in the case of a Poisson solid $\sigma = 0.25 (V_P = \sqrt{3}V_S, C_0 \sim 0.919402V_S)$ and a Gaussian source $f(t) = \exp(-\alpha(t - t_0)^2)$ with parameters $\alpha = 1000$ and $t_0 = 0.25$. Figure 4 depicts these signals and their features resulting from the arrivals of the P wave at time $T_{P;R2} \sim 3.8$ sec, S wave at time $T_{S;R2} \sim 6.6$ sec, and Rayleigh pulse $T_{R;R2} \sim 7.2$ sec.

In particular, the inset in figure 4 shows u_{R2}^{AN} decaying to very low magnitudes during the time interval $(T_{S;R2}, T_{R;R2})$ of approximately 0.58 sec, as a result of the natural separation of the S and Rayleigh waves with the increase of the propagation distance. Conversely, waveform w_{R2}^{AN} does not present a similar separation behavior at any of deployed receivers in our test. Thus, we define a cut-off time $T_{CUT;R2}$ to truncate the time series $u_{R2}^{AN}(t_k)$ and keep records for $t_k \geq T_{CUT;R2}$ that only describe the Rayleigh pulse, and guarantees that the energy content of $u_{R2}^{AN}(t_k \geq T_{CUT;R2})$ does not have any interference from P or S waves. An obvious definition for $T_{CUT;R2}$ corresponds to the discrete time t_k at which $u_{R2}^{AN}(t_k)$ reaches its minimum magnitude in

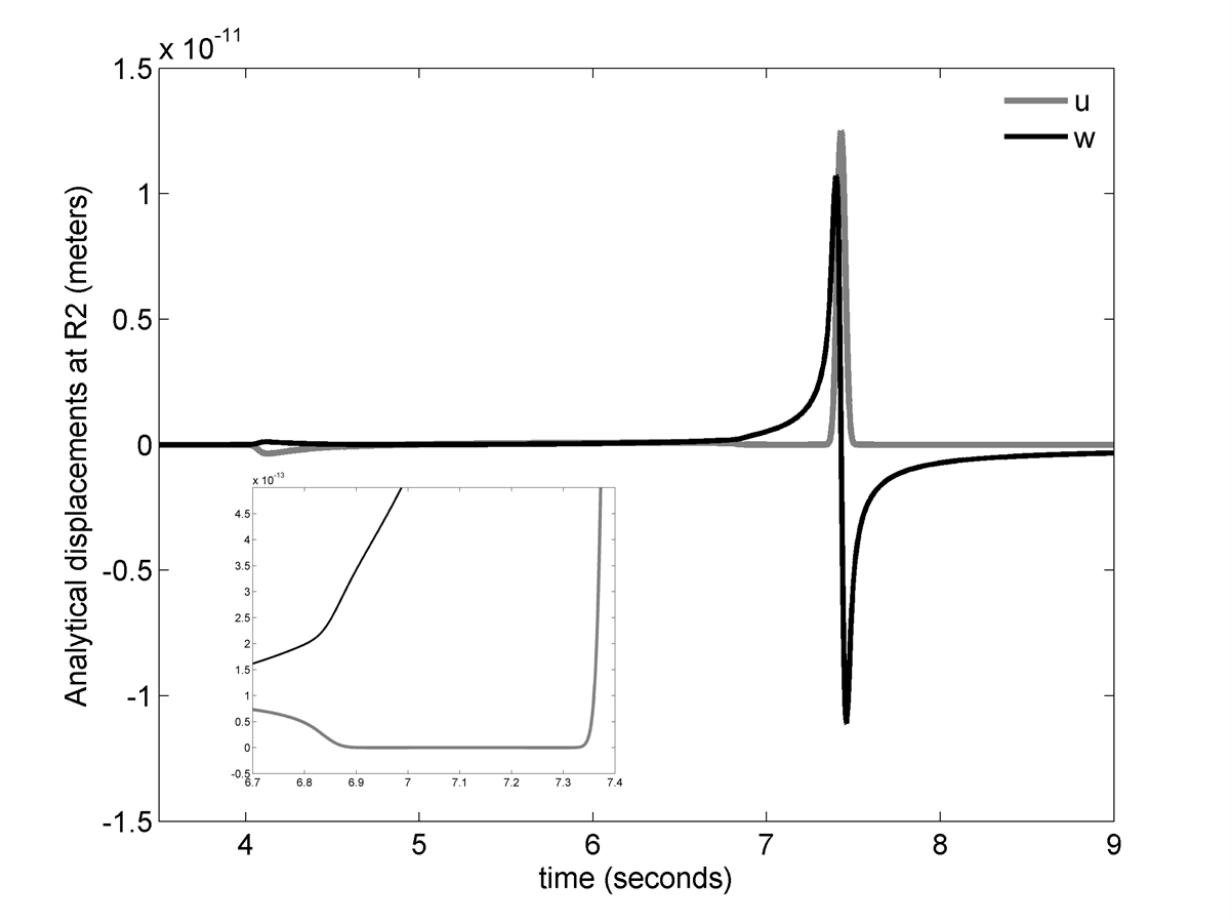

Fig. 4: Horizontal u (grey line) and vertical w (black line) analytical displacements at surface receiver R2. The domain is a Poisson solid with a S wave speed of $V_S = 2000m/s$. Arrival times of P, S, and Rayleigh waves at this location are approximately 3.8 sec, 6.6 sec, and 7.2 sec, respectively

the interval $(T_{S;R2}, T_{R;R2})$, and we take the first occurrence of such minima in case of non-uniqueness. Our definition of $T_{CUT;R2}$ for $t_k \in (T_{S;R2}, T_{R;R2})$ is

$$T_{CUT;R2} = \min\{t_k^i : u_{R2}^{AN}(t_k^i) = \min|u_{R2}^{AN}(t_k)|\} \qquad (15)$$

Then, we take the truncated waveform $u_{R2}^{AN}(t_k \geq T_{CUT;R2})$ as the windowed Rayleigh pulse at receiver R2 which represents the output of *STEP I* of our dispersion analysis. The need of keeping all signal records $u_{R2}^{AN}(t_k)$ for $t_k \geq T_{CUT;R2}$ in windowed waveforms arises from dispersion anomalies observed on numerical displacement seismograms. Recall that the purpose of this dispersion analysis is to serve as a metric for comparing FS numerical implementations.

Figure 5 depicts VPSG and MPSG windowed Rayleigh waves at location R2 and compares those with the analytical windowed pulse. In these numerical waveforms, we observe the amplitude reduction of the pulse Rayleigh and how the low grid-sampling of its high frequency components delays these modes which end up trailing the main pulse. This anomalous behavior is typical of second- (and lower-) order discretizations of FS boundary conditions. Thus, a complete analysis of Rayleigh pulses on numerical waveforms must allow for simulation time long enough that most of these oscillations reach the recording receiver. Figure 5 also shows the MSSG windowed Rayleigh pulse at receiver R2. Note that it exhibits dispersion-driven oscillations both preceding and following the main pulse, illustrating that numerical dispersion leads to higher and slower speeds than the exact Rayleigh velocity. As a result, it is likely that the discrete time $T_{CUT;R2}$ in eqn. (15) may not be unique on fourth-order simulations of Rayleigh waves.

The second step of our dispersion analysis focuses on computing the horizontal displacements **u** at receiver R1, and then windowing the Rayleigh pulse on a time series with equal length to that previously obtained R2. This windowing process proceeds well if the time gap

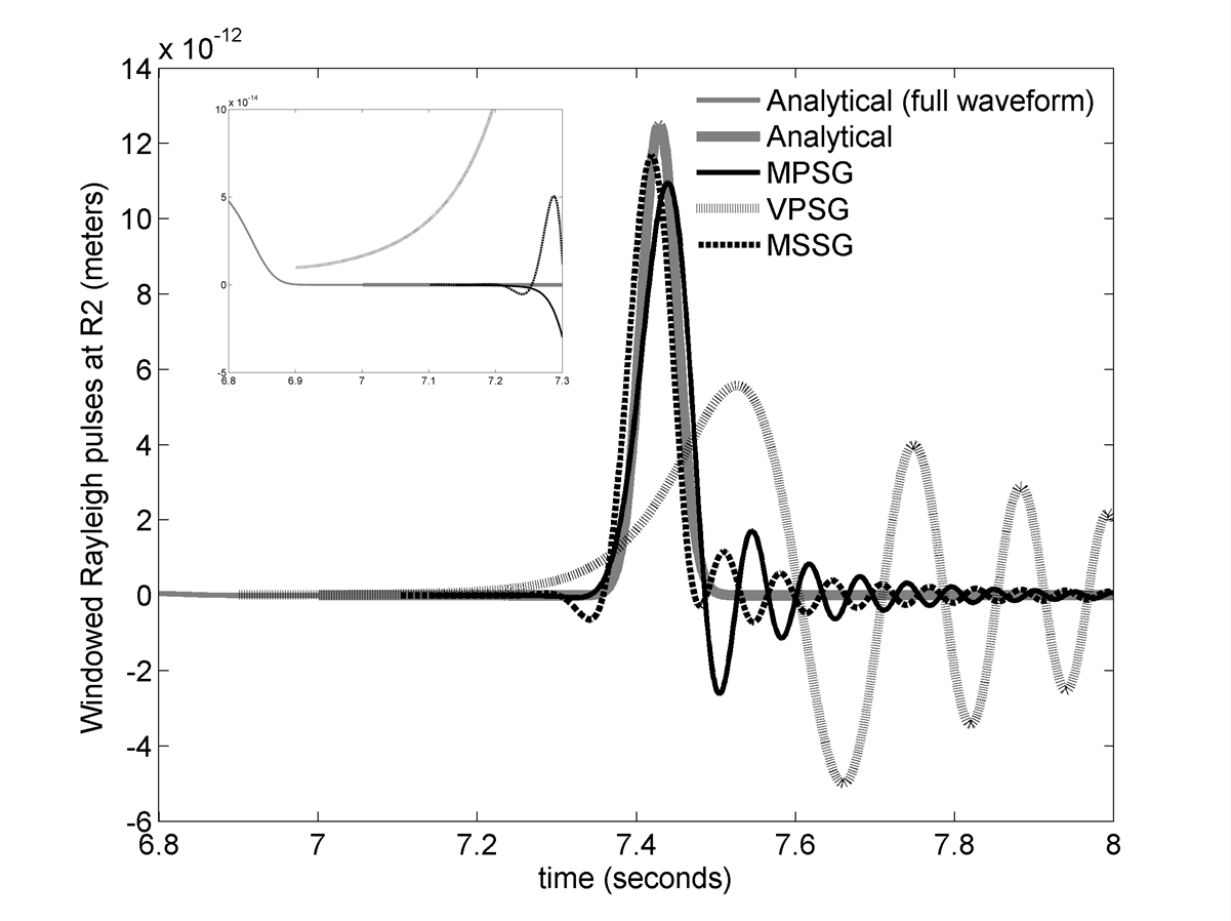

Fig. 5: Windowed Rayleigh pulses on all available (Analytical - thick grey signal -, VPSG, MSSG, and MPSG) time series at surface receiver R2. As a reference, the full analytical waveform (thin grey curve) is also depicted to show P- and S-wave features. Simulations for second-order MPSG and VPSG schemes use a grid size of $h = 10$ m, while fourth-order MSSG method employs $h = 25$ m

($T_{R;R1}$ - $T_{S;R1}$) is approximately 0.5 sec (or higher). The third and final step follows the usual two-station dispersion analysis of surface waves that estimates the dispersion curve $C(f)$ from the phase difference of windowed Rayleigh pulses at R2 and R1 once transformed to the frequency domain via *fft*. We summarize this procedure in the following sketch (Algorithm 2), making specific references to analytical time series and receivers R1 and R2, although this algorithm applies to any receiver pair (with the exception of $R0$ where $T_{R;R1}$ - $T_{S;R1} \sim 0.2$ sec).

In *STEP III*, w represents the angular frequency, Δx is the distance between stations R1 and R2, and phase unwrapping allows getting a smooth dispersion curve $C(f)$. The unwrap routine provided by MATLAB R2011 yields smooth phases in the frequency range of source excitation in our tests. For instance, in our current test 99% of the source energy lies below 25hz, and MATLAB unwrapping yields smooth phases up to this frequency.

Algorithm 2 DCR algorithm

STEP I: Obtain windowed Rayleigh pulse at R2, $u^{AN}_{R2}(t_k \geq T_{CUT;R2})$ for $T_{C;R2}$ given by eqn. (15). Compute phase spectrum $\varphi_{R2}(f)$ via *fft*.
STEP II: Obtain an equally long windowed Rayleigh pulse at R1, $u^{AN}_{R1}(T_{SIZE} \geq t_k \geq T_{CUT;R1})$ for $T_{C;R1}$ given by eqn. (15) and T_{SIZE} chosen such that *length*{*windowed pulse at R1*} = *length*{*windowed pulse at R2*}. Compute phase spectrum $\varphi_{R1}(f)$ via *fft*.
STEP III: Calculate dispersion curve $C(f)$ from the difference of unwrapped phases $\varphi^{un}_{R2}(f)$ and $\varphi^{un}_{R1}(f)$ [20]:

$$\varphi^{un}_{R2}(f) - \varphi^{un}_{R1}(f) = w\Delta x\left[\frac{T_{CUT;R2} - T_{CUT;R1}}{\Delta x} + \frac{1}{C(f)}\right]$$

Figure 6 presents normalized dispersion curves $\frac{C(f)}{C_0}$ estimated by the DCR algorithm using as input all (analytical, VPSG, MSSG, and MPSG) time series avail-

able at receivers R1 and R2 in this test where $\sigma = 0.25$. Consistency of this algorithm is empirically proven by the fact that $C(f) = C_0$, within round-off errors, in the case of analytical displacements. In this figure, we also observe phase speed distortions obtained by DCR from all numerical schemes under comparison. Setting 5% as an acceptable dispersion error for Rayleigh wave propagation, VPSG approximately requires 13.3 nodes per $\lambda^S(\frac{h}{\lambda^S} \sim 0.075)$, whereas MPSG demands close to 6.6 nodes per $\lambda^S(\frac{h}{\lambda^S} \sim 0.15)$, i.e. the half of grid points required by VPSG. On the other hand, if we reduce the tolerance to 1% of dispersion error, MSSG achieves this accuracy target using only 4 nodes per λ^S $(\frac{h}{\lambda^S} \sim 0.25)$, while MPSG requires grid densification by a factor of two and a half, to 10 points per λ^S $(\frac{h}{\lambda^S} \sim 0.1)$ (see inset in fig. 6). Traditional FD SSG implementations of planar FS based on either the mixed-order (a combined use of fourth- and second-order accurate stencils) image method or the fully fourth-order AFDA methods proposed by Kristek and co-workers, model surface wave propagation with low dispersion errors under a grid resolution of 10 or 6 grid points per minimum λ^S, respectively ([16][15][19]). Using such grid sampling criteria as references, we approximate the dispersion errors for each numerical method as shown in figure 6 and present them in table 1. Note that VPSG errors are consistently four times higher than those deliver by the MPSG scheme under same grid sampling, while the MSSG method shows a remarkable accuracy yielding negligible errors compared to those observed on MPSG solutions.

Table 1: Approximate dispersion errors of numerical schemes VPSG, MSSG, and MPSG, in the cases of grid sampling ratio of 10 and 6 nodes per S wavelength λ^S (taken from figure 6). Tests are performed on a Poisson solid ($\sigma = 0.25$) for the Gaussian point source $f(t) = \exp(-1000(t - 0.25)^2)$

Scheme	Dispersion error	
	10 nodes per λ^S	6 nodes per λ^S
VPSG	8%	20%
MSSG	0.125%	0.125%
MPSG	2%	5%

5.2 Sensitivity of the DCR Algorithm

In this section, we verify the consistency of the DCR algorithm by reproducing the dispersionless propagation of exact Rayleigh waves on a set of Lamb's problems carried out for different Poisson ratios σ, and a variety of point sources. First, we consider σ of 0.20, 0.30, and 0.35, that combine with the test discussed above with $\sigma = 0.25$, to cover the range of Poisson ratio observed on most crustal rocks. Source excitation is kept fixed as the Gaussian $f(t) = \exp(-1000(t - 0.25)^2)$. The constant speed C_0 of all Rayleigh wave components is a known function of V_S and σ, and given by the unique real root of the following cubic equation that satisfies $C_0 < V_S$ (i.e., [20]),

$$\varepsilon^3 - 8\varepsilon^2 + \left(24 - \frac{16}{k}\right)\varepsilon - 16\left(1 - \frac{1}{k}\right) = 0$$

where $\varepsilon = (\frac{C_0}{V_S})^2$, and $k = \frac{2(\sigma-1)}{2\sigma-1}$.

Table 2 presents six-digit approximations to $\sqrt{\varepsilon}$ for the representative set of σ values under consideration. Notice that the increase of σ implies the decrease of the time gap between S and Rayleigh wave arrivals at the surface location R1, $(T_{R;R1} - T_{S;R1})$, and then reduces the set of signal samples available to define the cut-off time $T_{CUT;R1}$. However, in the case of $\sigma = 0.35$, we find that a time gap $(T_{R;R1} - T_{S;R1})$ of approximately 0.4 sec is long enough to pick appropriate cut-off times at both receivers R1 and R2 in *STEP I* and *STEP II* of the DCR algorithm, respectively.

Table 2: Proportionality between Rayleigh wave speed (C_0) and S-wave speed (V_S) for different Poisson's ratios: $C_0 = V_S\sqrt{\varepsilon}$

σ	$\sqrt{\varepsilon}$
0.20	0.910996
0.25	0.919402
0.30	0.927413
0.35	0.935013

Figure 7a shows the dispersion curves calculated by the DCR algorithm using the analytical surface displacements when three alternative values (to $\sigma = 0.25$) are used for the Poisson ratio ($\sigma = 0.20$, 0.30, and 0.35). This figure illustrates the consistency and applicability of DCR to Lamb's problems on materials with σ ranging in [0.20, 0.35].

We also explore the sensitivity on the source time shape of the Rayleigh-pulse windowing process that highly depends on cutting-off times and equation (15) (used in *STEPS I* and *II* of the DCR algorithm). The consistency of the DCR algorithm also relies on this isolation process. Thus, we consider three alternative point sources to the Gaussian shape used above, and

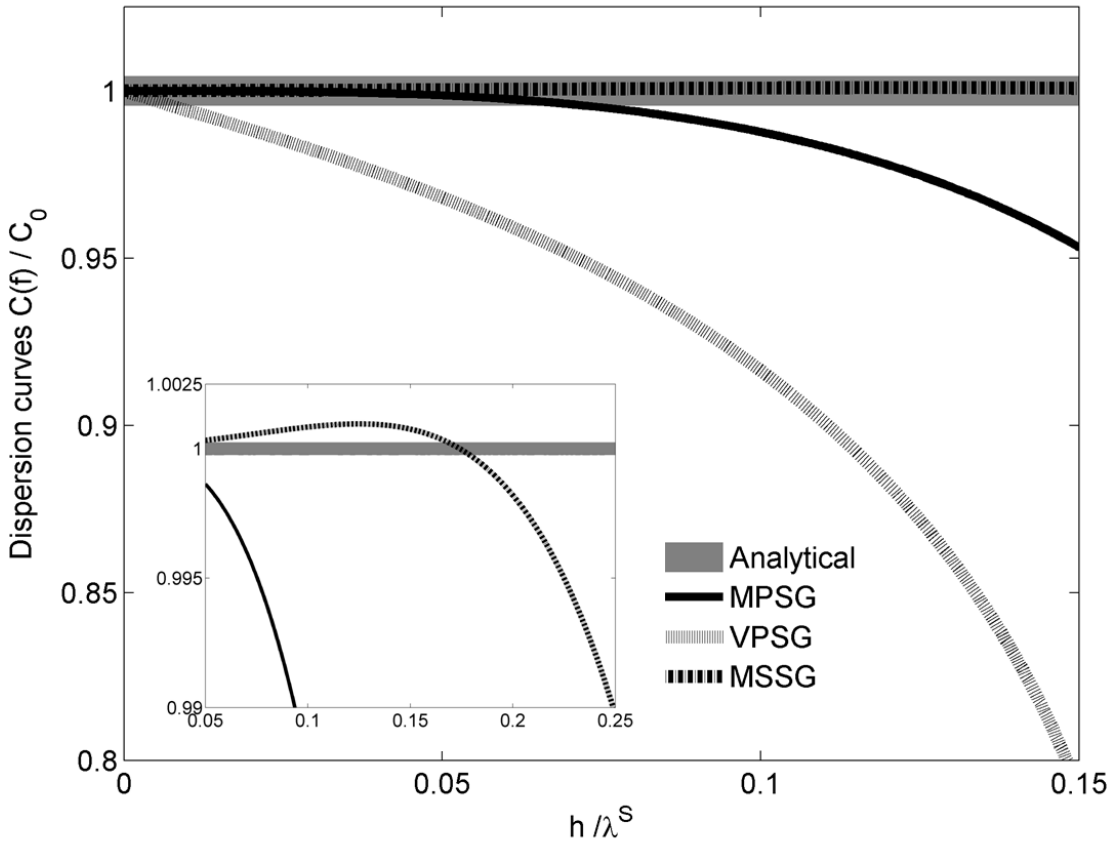

Fig. 6: Normalized dispersion curves of windowed Rayleigh waves on all available solutions (Analytical, VPSG, MSSG, and MPSG) estimated by the DCR algorithm. DCR uses time series recorded at surface receivers R1 and R2 and shown in figure 5

compute the analytical free-surface displacements in the case of Poisson half space ($\sigma = 0.25$). From those commonly used in numerical seismological applications, we opt for the Gaussian derivative $g(t) = -2\alpha(t - t_0)\exp(-\alpha(t - t_0)^2)$ ($\alpha = 1000$, $t_0 = 0.25$), the Gabor wavelet $h(t) = \exp(\frac{-\beta_G^2}{\delta^2})\cos(\beta_G + \theta)$ where $\beta_G = 2\pi f_p(t - t_0)$ ($f_p = 12.5\ hz$, $\delta = 5$, $\theta = \frac{\pi}{2}$), and the Ricker function $k(t) = (\frac{\sqrt{\pi}}{2})(\beta_R - 0.5)\exp(-\beta_R)$ where $\beta_R = (\pi\frac{(t-t_0)}{t_p})^2$ ($t_p = 0.125\ s$). The parameter values for these three alternative source models have been chosen to their energy spectrum to frequencies below about 25 hz, making them comparable in this respect to the Gaussian source used previously. Figure 8 compares the source spectra. Figure 7b reveals the low sensitivity of the Rayleigh-pulse windowing process of DCR on the particular time shape on the point source, and confirms the natural separation of this pulse from body waves traveling ahead on this benchmark Lamb's problem.

5.3 Time-dependent error analysis and numerical convergence

We next briefly examine accuracy and convergence properties of numerical solutions to the Lamb's problem under grid refinement, and use the RMS metric given in eqn. (14) to quantify error. To do so, we again use the numerical test with the Gaussian point source $f(t) = \exp(-1000(t - 0.25)^2)$. As a reference measure of the maximum frequency of the source energy, we take the 99% percentile of its amplitude spectrum, which gives $f_{MAX} \sim 22\ hz$. Thus, the minimum S wavelength is about $\lambda^S_{min} \sim 91\ m$ ($V_S = 2000\ \frac{m}{s}$), and we use this distance as a reference length scale. Among the eight free-surface receivers available in this test (see figure 3), we compute RMS misfits at receivers R0 and R2, corresponding to propagation distances of approximately $53\lambda^S_{min}$ and $145\lambda^S_{min}$, respectively. Waveform anomalies caused by numerical dispersion, such as high-frequency

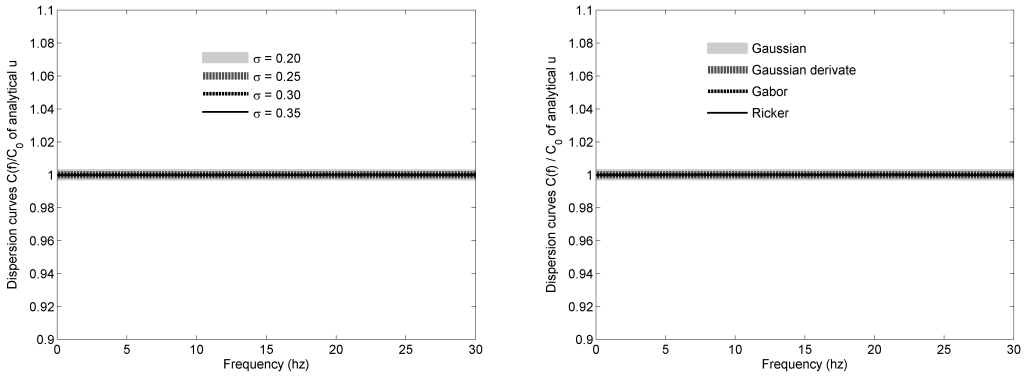

(a) (b)

Fig. 7: Normalized dispersion curves estimated by the DCR algorithm for the analytical time series at surface receivers R1 and R2. (a) The point source corresponds to the Gaussian model depicted in figure 8, and tests are performed the four different Poisson ratios $\sigma = 0.20$, 0.25, 0.30, and 0.35. (b) The domain is a fixed Poissonan homogeneous halfplane, and tests are performed for the four different point source models depicted in figure 8

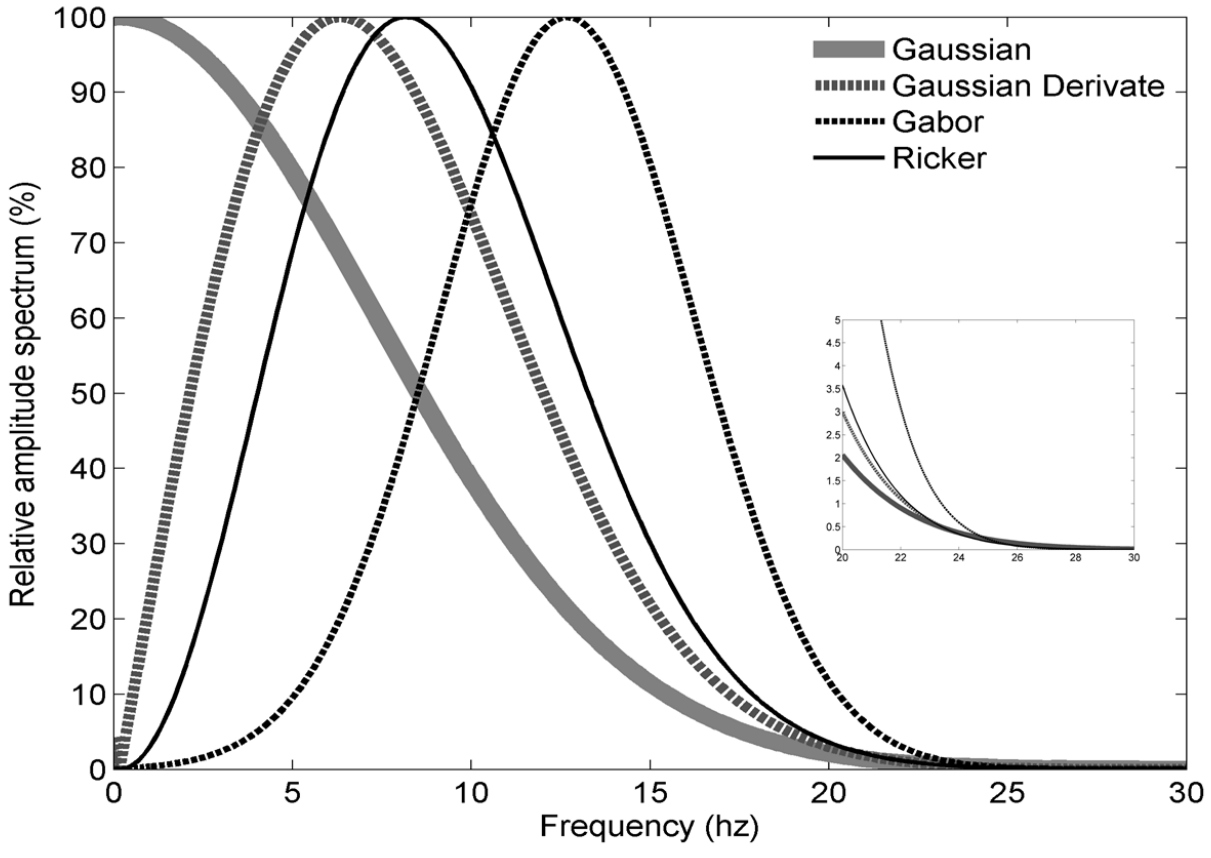

Fig. 8: Percentage amplitude spectrum of four different point sources used to test the consistency of the DCR algorithm under variation of the time shape of the Rayleigh pulse

oscillations and time shifts of peak values, lead naturally to a cumulative accuracy degradation with propagation distance, and we here compare RMS misfits at R0 and R2 as a way to assess this affect (also, its implications on convergence rates can be assessed). For each of the competing schemes (VPSG, MSSG, and MPSG), we perform ten simulations on square grids using the steps $h = 10, 15, 22, 25, 30, 40, 50, 60, 80$, and 100 m, and time steps given by $\Delta t = 0.5\frac{h}{V_P}$ that satisfies CFL stability constraints on both grids PSG and SSG (see eqn. (9) and Appendix B). To give a better physical interpretation of error behavior, we relate the grid spacing h to the minimum wavelength λ^S_{min} and define grid resolution as the number of gridpoints N_λ fitted into this distance, i.e., $N_\lambda = \frac{\lambda^S_{min}}{h}$. Thus, in our simulations the grid-resolution parameter N_λ varies in the range $0.9 \leq N_\lambda \leq 9$. We refer to computational meshes with $N_\lambda < 3$ as poorly-resolved grids given that the number of gridpoints sampling wavelengths near to λ^S_{min} is close to theoretical Nyquist limit ($N_\lambda = 2$). On the other hand, we call well-resolved those grids where $N_\lambda \geq 6$ to be consistent with published fourth-order AFDA simulations of surface waves on 3-D SSG where satisfactory accuracy is achieved if $\frac{\lambda^S_{min}}{h} \geq 6$ [19].

We now compare accuracy achieved by VPSG, MSSG, and MPSG in figures 9a and 9b, where grey symbols represent misfits at farther receiver R2 and black symbols correspond to misfits at closer receiver R0. We estimate the order of convergence of these solutions by linear least-square fitting of RMS misfits on the logarithmic scale used on figures 9a and 9b, and fitted slopes are given in table 3. In these figures, we also plot a solid line that represents a perfect quadratic convergence (scaling with h^2), as a graphical reference for the decrease of RMS misfits with h. On poorly-resolved grids ($N_\lambda \leq 2.3$), VPSG and MPSG misfits nearly exceed 100% for both displacements, and we attribute this inaccurate behavior to the second-order (in case of MPSG) and lower-order (in case of VPSG) treatment of the FS boundary condition. As grid resolution improves, the sub-linear convergence of VPSG (see table 3) inhibits any significant accuracy gain for the range of grid spacing explored in these tests.

Our VPSG results are consistent with precision studies presented by Bohlen and Saenger in [3], where accurate modeling of Rayleigh propagation is accomplished for 30 grid points sampling λ^P (i.e., 17 grid points per λ^S in a Poisson solid). Conversely, the faster convergence (from super linear to just linear) of MPSG leads to a more rapid decrease of RMS misfits that barely exceed 10% on well-resolved grids ($N_\lambda \geq 9$) and nearly match the precision of MSSG (more evident in displacement w).

Table 3: Approximate convergence rates under grid refinement of solutions computed by VPSG, MSSG, and MPSG schemes to exact displacements u and w at surface receivers R0 and R2

Scheme	Convergence rates of numerical solutions to u		Convergence rates of numerical solutions to w	
	at R0	at R2	at R0	at R2
VPSG	0.48	0.21	0.35	0.14
MSSG	0.98	0.92	1.78	1.45
MPSG	1.55	1.01	1.35	0.95

Figures 9a and 9b also indicate that MPSG errors for both displacements may actually scale (with h) differently according to the grid-resolution range. That is, MPSG errors decay sub-linearly on low-resolved grids, with a transition to quadratic convergence on better-resolved grids ($N_\lambda \geq 3$) with a better realization in the case of the closer receiver R0 (consistent with MPSG second-order nominal accuracy). Next, we focus on accuracy and convergence properties of MSSG displacement solutions computed at receivers R0 and R2 and therefore valid for propagation distances up to approximately $145\lambda^S_{min}$. On coarse grids ($N_\lambda \leq 1.5$), MSSG misfits are higher than 30% for both displacement components, but the superlinear convergence of this scheme in the case of w renders higher accuracy on moderately resolved grids ($N_\lambda \geq 3$) where misfits are below 10%. Similar accuracy target on displacement u is achieved by MSSG only on very fine grids ($N_\lambda \geq 9$) in response to the slower linear convergence on this field. The fact that MSSG scheme models displacement w more precisely than it does component u is consistent to the H-formulation of FS boundary conditions on SSG published by Gottschammer and Olsen [15] and Kristek et al. [19]. These independent algorithms model phases of the displacement (or velocity) component normal to the free-surface more accurately than phases of both tangential displacements (or velocities). On the other hand, this accuracy discrepancy on solutions to both displacement components is not observed in our results on PSG. Misfits on u are comparable to misfits on w at the same grid spacing h, when either VPSG or MPSG errors are qualitatively compared across figures 9a and 9b. This observation suggests that dispersion-driven anomalies on u waveforms become more significant that those affecting w waveforms on SSG, and further motivates the application of the DCR dispersion analysis to the former displacement component in order to measure phase speed distortions.

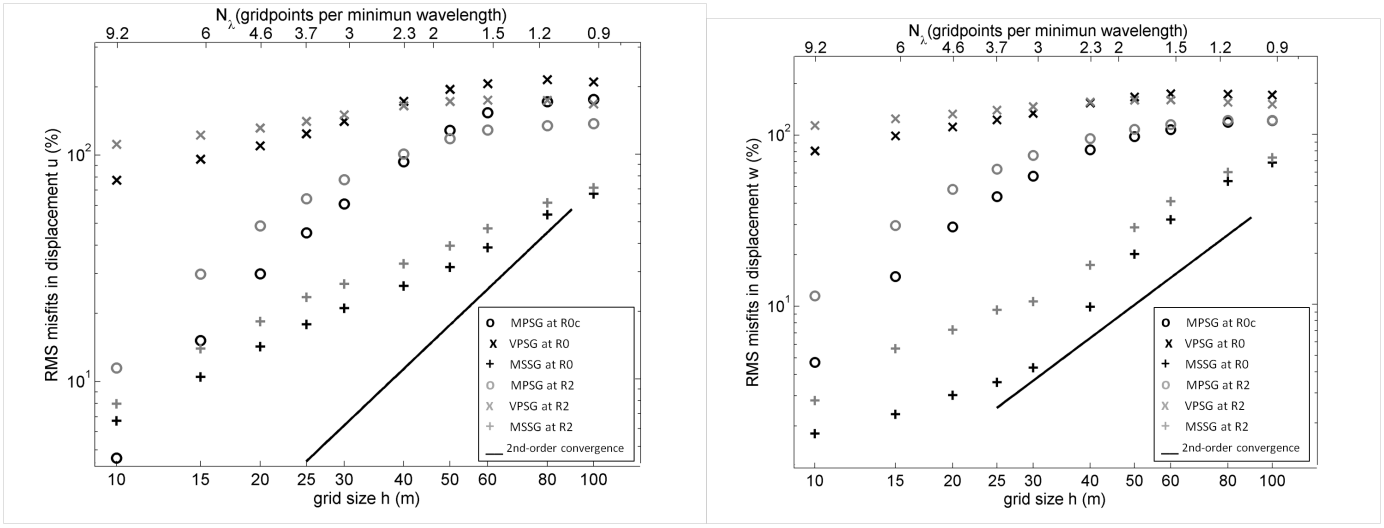

(a) (b)

Fig. 9: Relative RMS misfits of VPSG, MSSG, and, MPSG solutions to analytical displacements u (chart a) and w (chart b), at free-surface receivers R0 (black symbols) and R2 (grey symbols). Grid spacing h varies in the range $10\,m \leq h \leq 100\,m$ along the bottom axis, and the number of grid points sampling the S wavelength measures the grid resolution in the top axis

6 Conclusion

In this paper, we describe a new mimetic finite difference (FD) implementation of a planar free surface (FS) boundary condition on a 2-D elastic medium discretized by a partly staggered grid (PSG). This implementation (MPSG) places a new set of Compound nodes (displacement-stress nodes) along the FS gridline that allow the unilateral second-order discretization of null-traction conditions and the computation of all displacement and stress components. At interior gridpoints, spatial discretization of all wavefields is centrered and fourth-order accurate imitating PSG methods that employ the vacuum-layer implementation of FS boundaries (VPSG methods). We next approximate the dispersion curves of both schemes on a Lamb's experiment by computing the phase difference of isolated Rayleigh pulses (from body wave arrivals) at two FS receivers. On PSG that fits either 6 or 10 gridpoints into a reference S wavelength λ^S, VPSG dispersion errors are four times higher than those delivered by the MPSG scheme. We additionally calculate root-mean-square (RMS) misfits of MPSG and VPSG time series relative to the analytical FS displacements for a variety of grid spacing h ($1 \leq \frac{\lambda^S_{MIN}}{h} \leq 9$). For epicentral distances ranging from $\sim 50\lambda^S_{MIN}$ to $\sim 130\lambda^S_{MIN}$, convergence of the former method degrades from super-linear to linear, and misfits barely exceed 10% in the case of $\frac{\lambda^S_{MIN}}{h} \approx 9$. In same tests, VPSG shows a much poorer convergence and delivers misfits higher than 70%.

To compare MPSG performance with a fully fourth-order accurate method on its spatial FD discretization (including FS nodes), we use the MSSG scheme that also employs mimetic stencils, but on a standard staggered grid. In our experiments, the former delivers comparable dispersion errors to the latter on twice denser grids. Along the explored range of epicentral distances, MSSG shows a slower RMS convergence in the case of the horizontal FS displacement that leads to a similar accuracy to MPSG on grids with $\frac{\lambda^S_{MIN}}{h} \approx 9$. However, MSSG models both displacement components more precisely on moderately resolved grids ($\frac{\lambda^S_{MIN}}{h} \leq 6$).

Acknowledgements Authors thank Dr. V. Cruz Atienza for his helpful comments on the "Vacuum" implementation of a planar free surface, and express our gratitude to Dr. Eric Dunham for providing a computational implementation of the Cagniard-De Hoop solution to the Lamb's problem. We also thank an anonymous reviewer for very thorough and helpful reviews. This work was supported by the National Science Foundation, under grants EAR-0810271, EAR-1135455 and EAR-9449443, by the HIPEAC European Network of Excellence and by the Ministry of Education of Spain under contract TIN2012-34557. Otilio J Rojas was funded by Universidad Central de Venezuela (CDCH) during his research stay at San Diego State University.

References

1. Aki, K., Richards, P.G.: Quantitative Seismology. W. H. Freeman and Co. San Francisco (1980)
2. Andrews, D.J.: A numerical study of tectonic stress release by underground explosions. Bulletin of the Seismological Society of America **63**, 1375–1391 (1973)
3. Bohlen, T., Saenger, E.H.: Accuracy of heterogeneous staggered-grid finite-difference modeling of rayleigh waves. Geophysics **71**(4), T109–T115 (2006)
4. Castillo, J., Grone, R.D.: A matrix analysis approach to higher-order approximations for divergence and gradients satisfying a global conservation law. SIAM Journal Matrix Analysis Applications **25**(1), 128–142 (2003). URL http://dx.doi.org/10.1137/S0895479801398025
5. Castillo, J.E., J.M.Hyman, Shashkov, M., Steinberg, S.: Fourth- and sixth-order conservative finite difference approximations of the divergence and gradient. Applied Numerical Mathematics: Transactions of IMACS **37**(1–2), 171–187 (2001)
6. Chen, W.Z.: Traction image method for irregular free surface boundaries in finite-difference seismic wave simulation. Geophysics Journal International **167**, 337–353 (2006)
7. Cruz-Atienza, V.M.: Personal communication on the implementation of the vacuum method on psg (2006)
8. Cruz-Atienza, V.M.: Rupture dynamique des faille nonplanaires en différences finies. Ph.D. thesis, Université de Nice, Sophia Antipolis (2006)
9. Cruz-Atienza, V.M., Virieux, J.: Dynamic rupture simulation of nonplanar faults with a finite difference approach. Geophysics Journal International **158**, 939–954 (2004)
10. Cruz-Atienza, V.M., Virieux, J., Aochi, H.: 3d finite-difference dynamic-rupture modelling along non-planar faults. Geophysics **72**, SM123–SM137 (2007)
11. Day, S.M.: Finite element analysis of seismic scattering problems. Ph.D. thesis, University of California, San Diego (1977)
12. Day, S.M.: Three-dimensional simulation of spontaneous rupture: the effect of nonuni- form prestress. Bulletin of the Seismological Society of America **72**(6A), 1881–1902 (1982)
13. Dong-Joo, M., Changsoo, S., Hai, S.Y.: Free-surface boundary condition in finite-difference elastic wave modeling. Bulletin of the Seismological Society of America **94**(1), 237–250 (2004)
14. Gelis, C., Leparoux, D., Virieux, J., Bitri, A., Operto, S., Grandjean, G.: Numerical modeling of surface waves over shallow cavities. Journal of Environmental and Engineering Geophysics **10**, 111–121 (2005)
15. Gottschammer, E., Olsen, K.B.: Accuracy of the explicit planar free-surface boundary condition implemented in a fourth-order staggered-grid velocity-stress finite-difference scheme. Bulletin of the Seismological Society of America **91**(3), 617–623 (2001)
16. Graves, R.W.: Simulating seismic wave propagation in 3d elastic media using staggered-grid finite differences. Bulletin of the Seismological Society of America **86**(4), 1091–1106 (1996)
17. Jih, R., McLaughlin, K., Der, Z.: Free-boundary conditions of arbitrary polygonal topography in a two-dimensional explicit finite-difference scheme. Geophysics **53**, 1045–1055 (1988)
18. andD. Kosloff, E.T.: 3d elastic modeling with surface topography by a chebychev spectral method. Geophysics **59**, 464–473 (1994)
19. Kristek, J., Moczo, P., Archuleta, R.J.: Efficient methods to simulate planar free surface in the 3d 4th-order staggered-grid finite-difference schemes. Studia Geophysica et Geodaetica **46**, 355–381 (2002)
20. Lay, T., Wallace, T.C.: Modern Global Seismology, vol. 58. Academic Press (1995)
21. Levander, A.: Fourth-order finite-difference p-sv seismograms. Geophysics **53**, 1425–1436 (1988)
22. Lombard, B., Piraux, J., Gélis, C., Virieux, J.: Free and smooth boundaries in 2-d finite-difference schemes for transient elastic waves. Geophysics Journal International **172**, 252–261 (2008)
23. Ma, S., Archuleta, R.J., Liu, P.: Hybrid modeling of elastic p-sv wave motion: A combined finite-element and staggered-grid finite-difference approach. Bulletin of the Seismological Society of America **94**(4), 1557–1563 (2004)
24. Madariaga, R.: Dynamics of an expanding circular fault. Bulletin of the Seismological Society of America **66**, 639–666 (1976)
25. Moczo, P., Kristek, J., Galis, M., Pazak, P., Balazovjech, M.: The finite-difference and finite-element modeling of seismic wave propagation and earthquake motion. Acta Physica Slovaca **52**(2), 177–406 (2007)
26. Moczo, P., Kristek, J., Halada, L.: 3d 4th-order staggered-grid finite difference schemes: stability and grid dispersion. Bulletin of the Seismological Society of America **90**, 587–603 (2000)
27. Moczo, P., Kristek, J., Halada, L.: The Finite-Difference Method for Seismologists. An Introduction. Comenius University, Bratislava (2004)
28. Olsen, K.B., Day, S.M., Minster, J.B., Cui, Y., Chourasia, A., Faerman, M., Moore, R., Maechling, P., Jordan, T.: Strong shaking in los angeles expected from southern san andreas earthquake. Geophysical Research Letters **33**(L07305), 1–4 (2006)
29. Pitarka, A.: 3d finite-difference modeling of seismic motion using staggered grids with nonuniform spacing. Bulletin of the Seismological Society of America **89**, 54–68 (1999)
30. Robertsson, J.: A numerical free-surface condition for elastic / viscoelastic finite-difference modeling in the presence of topography. Geophysics **61**, 1921–1934 (1996)
31. Rodrigues, D.: Large scale modelling of seismic wave propagation. Ph.D. thesis, Centrale Paris' Ecole, Paris (1993)
32. Rojas, O.: Mimetic finite difference modeling of 2d elastic p-sv wave propagation. Research Report CSRCR2007-05, Computational Science Research Center, San Diego State University (2007)
33. Rojas, O., Day, S.M., Castillo, J.E., Dalguer, L.A.: Modelling of rupture propagation using high-order mimetic finite differences. Geophysical Journal International **172**(2), 631–650 (2008). DOI 10.1111/j.1365-246X.2007.03651.x. URL http://dx.doi.org/10.1111/j.1365-246X.2007.03651.x
34. Rojas, O., Dunham, E., Day, S.M., Dalguer, L.A., Castillo, J.E.: Finite difference modeling of rupture propagation with strong velocity-weakening friction. Geophysical Journal International **179**, 1831–1858 (2009). DOI doi:10.1111/j.1365-246X.2009.04387.x
35. Saenger, E.H., Bohlen, T.: Finite-difference modeling of viscoelastic and anisotropic wave propagation using the rotated staggered grid. Geophysics **69**, 583–591 (2004)
36. Saenger, E.H., Gold, N., Shapiro, S.A.: Modeling the propagation of elasticwaves using a modified finite-difference grid. Wave Motion **31**, 77–92 (2000)

37. Virieux, J.: Sh wave propagation in heterogeneous media: Velocity-stress finite-difference method. Geophysics **49**, 1933–1957 (1984)
38. Virieux, J.: P-sv wave propagation in heterogeneous media: Velocity-stress finite-difference method. Geophysics **51**, 889–901 (1986)
39. Zahradnik, J., Moczo, P., Hron, F.: Testing four elastic finite-difference schemes for behaviour at discontuities. Bulletin of the Seismological Society of America **83**(1), 107–129 (1993)
40. Zhang, J.: Quadrangle-grid velocity-stress finite-difference method for elastic- wave-propagation simulation. Geophysics Journal International **131**(1), 127–134 (1997). DOI 10.1111/j.1365-246X.1997.tb00599.x

A Mimetic Finite Difference Operators

Castillo-Grone mimetic FD operators are designed to perform numerical differentiation on a 1-D SG and discrete approximations preserve an integration-by-part formula (including boundary terms). This conservative property motivates the acronyms *mimetic*. On the interval $[0, a]$, let us consider evaluations of two smooth functions $f(z)$ and $v(z)$ on the SG shown by figure 10. For an equal-sized partition of N cells (by step $h = \frac{a}{N}$) this grid comprises nodes $z_j = jh$, $j = 0, 1, \ldots, N$ and cell centers $z_{j+\frac{1}{2}} = \frac{z_j + z_{j+1}}{2}$, $j = 0, 1, \ldots, N-1$. Evaluations of f at cell centers and boundary points are collected in vector **f**, while evaluations of v at nodes are accommodated in vector **v**, i.e.,

$$f = (f(z_0), f(z_{\frac{1}{2}}), \ldots, f(z_{N-\frac{1}{2}}), f(z_N))$$

$$v = (v(z_0), v(z_1), \ldots, v(z_N))$$

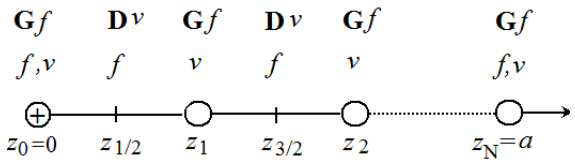

Fig. 10: 1-D staggered grid for mimetic finite differentiation of functions f and v using the difference operators G and D, respectively. Locations of vector evaluations $f = (f(z_0), f(z_{\frac{1}{2}}), \ldots, f(z_{N-\frac{1}{2}}), f(z_N))$ and $v = (v(z_0), v(z_1), \ldots, v(z_N))$ are shown, as well as sites of approximations $(Gf)_j$ and $(Dv)_{j+\frac{1}{2}}$ (j integer)

FD approximations to $\frac{\delta f}{\delta z}$ and $\frac{\delta v}{\delta z}$, at grid locations also illustrated in figure 10, are given by Gf and Dv, respectively, where G and D are differentiation matrices corresponding to the following choices according to the desired order of accuracy [5], [4]:

Mixed-order case:

$$G_{2-4} = \frac{1}{h}\begin{pmatrix} -\frac{8}{3} & 3 & -\frac{1}{3} & 0 & 0 & 0 & 0\ldots \\ \frac{4}{39} & -\frac{31}{26} & \frac{44}{39} & -\frac{1}{26} & 0 & 0 & 0\ldots \\ 0 & \frac{1}{24} & -\frac{27}{24} & \frac{27}{24} & -\frac{1}{24} & 0 & 0\ldots \\ 0 & 0 & \frac{1}{24} & -\frac{27}{24} & \frac{27}{24} & -\frac{1}{24} & 0\ldots \end{pmatrix}$$

$$D_{2-4} = \frac{1}{h}\begin{pmatrix} -1 & 1 & 0 & 0 & 0 & 0 & 0\ldots \\ \frac{1}{23} & -\frac{26}{23} & \frac{26}{23} & -\frac{1}{23} & 0 & 0 & 0\ldots \\ 0 & \frac{1}{24} & -\frac{27}{24} & \frac{27}{24} & -\frac{1}{24} & 0 & 0\ldots \\ 0 & 0 & \frac{1}{24} & -\frac{27}{24} & \frac{27}{24} & -\frac{1}{24} & 0\ldots \end{pmatrix}$$

The order of accuracy of approximations $G_{2-4}f$ and $D_{2-4}v$ reduces from fourth at interior grid points to second in the vicinity of nodes z_0 and z_N.

Fourth-order case:

$$G_{4-4} = \frac{1}{h}\begin{pmatrix} \frac{47888}{14245} & \frac{1790}{407} & -\frac{14545}{9768} & \frac{8997}{16280} & -\frac{2335}{22792} & \frac{25}{9768} & 0\ldots \\ \frac{16}{105} & -\frac{31}{24} & \frac{29}{24} & -\frac{3}{40} & \frac{1}{168} & 0 & 0\ldots \\ 0 & \frac{1}{24} & -\frac{27}{24} & \frac{27}{24} & -\frac{1}{24} & 0 & 0\ldots \\ 0 & 0 & \frac{1}{24} & -\frac{27}{24} & \frac{27}{24} & -\frac{1}{24} & 0\ldots \end{pmatrix}$$

$$D_{4-4} = \frac{1}{h}\begin{pmatrix} \frac{4751}{5192} & \frac{909}{1298} & \frac{6091}{15576} & -\frac{1165}{5192} & \frac{129}{2596} & -\frac{25}{15576} & 0\ldots \\ \frac{1}{24} & -\frac{27}{24} & \frac{27}{24} & -\frac{1}{24} & 0 & 0 & 0\ldots \\ 0 & \frac{1}{24} & -\frac{27}{24} & \frac{27}{24} & -\frac{1}{24} & 0 & 0\ldots \\ 0 & 0 & \frac{1}{24} & -\frac{27}{24} & \frac{27}{24} & -\frac{1}{24} & 0\ldots \end{pmatrix}$$

Approximations $G_{4-4}f$ and $D_{4-4}v$ are consistently fourth-order at all gridpoints.

B Mimetic Operators on a Standard Staggered Grid (MSSG scheme)

In this scheme, discretization of a 2-D elastic half-plane and associated wavefields proceeds on the rectangular SSG shown in figure 11. The grid has been enhanced by the inclusion of Compound nodes (displacement-stress gridpoints shown as filled symbols) along the FS to compute all wave fields at this boundary. Fourth-order differentiation along both directions (x, z) is used to approximate spatial derivates of stress components and displacement fields present in the equations of motion (eqns. (1) to (5)) and the FS condition (eqn. (6)). Thus, MSSG formulation relies on unilateral differentiation along z axis at the FS ($j = 0$) and horizontal gridlines nearby ($j = \frac{1}{2}, 1$), while centered stencils can be used for differentiation along both directions in any other case. Operators G_{4-4} and D_{4-4} provide an appropriate combination of one-sided and central FD SG stencils to implement this fourth-order MSSG method. Notice that the mimetic central stencil occupying inner rows of G_{4-4} and D_{4-4} corresponds to the standard fourth-order SG stencil that we here just referred as *central stencil* [21].

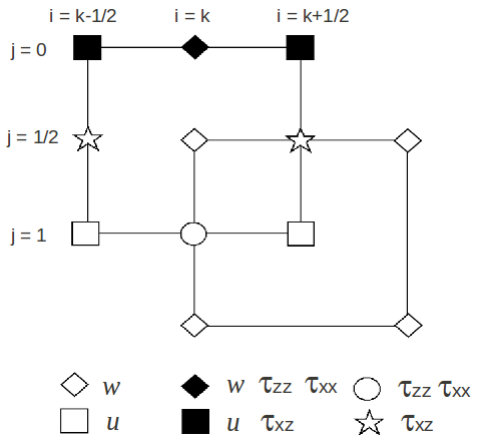

Fig. 11: 2-D rectangular staggered grid with $k = 1, 2, 3, \ldots$ and $i = \frac{1}{2}, 1, \frac{3}{2}, 2, \ldots$

In MSSG, time derivates in eqns. (1), and (2) are simply approximated by the nodal centered second-order FD stencil $\frac{1}{\Delta t^2} * (1, -2, 1)$, for Δt the time step. In a square SSG, the common grid step Δh in both directions constrains the size of Δt through the Von-Neumann stability condition presented by Levander [21] for fourth-order FD schemes in 2-D infinite media given by $\Delta t V_P \Delta h^{-1}\sqrt{2} \leqslant (\Sigma_{K=1}^{n}|C_K|)^{-1}$. The following pseudocode (Algorithm 3) sketches a MSSG time iteration from discrete time $t = n\Delta t$ to $t = (n+1)\Delta t$ by assuming that displacements u and w are available at the former time level.

MSSG calculations at interior gridlines $j = \frac{3}{2}, 1, \ldots$, replicates standard elastic solvers that use the fourth-order central stencil for spatial differentiation (for instance, the velocity-stress scheme of Levander [21]), in combination to second-order time discretization of the equations of motion as referred in *STEPS IV* and *V*.

Algorithm 3 MSSG scheme

Computation of tensor stress components τ_{xx}, τ_{zz} and τ_{xz} at time $t = n * \Delta t$

STEP I (for any integer i): Calculate $u_{\prime x}$ with the central stencil in the cases of $j = 0, 1$. For $j = 0$, FS condition $\tau_{zz} = 0$ implies that $w_{\prime z} = -\gamma * u_{\prime x}$ where $\gamma = \frac{\lambda}{(\lambda+2*\mu)}$. In the case of $j = 1$, compute $w_{\prime z}$ by using the unilateral stencil $(g_{21}, g_{22}, g_{23}, g_{24}, g_{25})$ (second row of G_{4-4}). Finally, obtain stresses τ_{xx} and τ_{zz} by means of Hooke's law along horizontal gridlines $j = 0, 1$ (note that $\tau_{zz} = 0$ at $j = 0$).

STEP II (for any half-integer i): In the case of $j = \frac{1}{2}$, compute $w_{\prime x}$ and $u_{\prime z}$ by using the central stencil and unilateral stencil $(d_{11}, d_{12}, d_{13}, d_{14}, d_{15}, d_{16})$ (first row of D_{4-4}), respectively. Then, Hooke's law yields τ_{xz}. For $j = 0$, the FS boundary condition enforces $\tau_{xz} = 0$.

Computation of horizontal displacement u at time $t = (n + 1) * \Delta t$

STEP III (for any half-integer i): Calculate $\tau_{xx'x}$ with the central stencil along horizontal gridlines $j = 0, 1$. For $j = 0$, compute $\tau_{xz'z}$ with the unilateral stencil $(g_{11}, g_{12}, g_{13}, g_{14}, g_{15}, g_{16})$, (first row of D_{4-4}), whereas stencil $(g_{21}, g_{22}, g_{23}, g_{24}, g_{25})$ allows obtaining this term in the case of $j = 1$.

STEP IV (for any half-integer i): For $j = 0, 1$, calculate the acceleration term $A_{ij} = rho^{-1} * (\tau_{xx'x} + \tau_{xz'z})$ and update displacement u according to equation (1), i.e., $u^{n+1} = 2 * u^n - u^{n-1} + \Delta t^2 * A_{ij}$.

Computation of vertical displacement w at time $t = (n + 1) * \Delta t$

STEP V (for any integer i): In the case of $\frac{1}{2}$, calculate $\tau_{xz'x}$ by using the central stencil and compute $\tau_{zz'z}$ with the unilateral stencil $(d_{11}, d_{12}, d_{13}, d_{14}, d_{15}, d_{16})$. Then, evaluate the acceleration term $A_{ij} = \rho^{-1} * (\tau_{xz'x} + \tau_{zz'z})$ and obtain displacement w^{n+1} in a similar way used in *STEP IV* (w replace u).

STEP VI (for any integer i): For $j = 0$ compute $u_{\prime x}$ at time $t = (n + 1) * \Delta t$ using the central stencil applied to neighbor values u^{n+1}. The term $w_{\prime z}$ present in the condition $\tau_{zz} = 0$ and written as $w_{\prime z} = -\gamma * u_{\prime x}$, in *STEP I*, is discretized by means of unilateral stencil $(g_{11}, g_{12}, g_{13}, g_{14}, g_{15}, g_{16})$ and value w^{n+1} results from this identity. This calculation uses previously computed w values at interior grid points at level time $t = (n+1)*\Delta t$.